Applying Multi-Objective Variable-Fidelity Optimization Techniques to Industrial Scale Rotors: Blade Designs for CleanSky

Gunther Wilke
German Aerospace Center (DLR) Braunschweig, Institute of Aerodynamics and Flow Technology
Lilienthalplatz 7, 38108 Braunschweig, Germany, gunther.wilke@dlr.de

Abstract

A novel variable-fidelity multi-objective optimization technique is applied to the design problem of helicopter rotorblades of the Green RotorCraft research programme of CleanSky. The optimization technique utilizes information from aerodynamic low-fidelity tools, here a prescribed wake model in forward flight and inviscid CFD simulations in hover, to speed-up the high-fidelity optimization, which is based on RANS simulations including all five-rotor blades. In reference to a state-of-the-art single-fidelity optimization, this approach finds about 325% more viable data points. A choice of three rotorblades from the final Pareto frontier of the optimization is investigated in detail including the off-design performance as well as acoustic footprint in an overflight condition. The final outcome is that there does not exist one blade that fully satisfies all criteria at once, but feasible trade-offs are found when applying the variable-fidelity multi-optimization technique.

1 INTRODUCTION

The Cleansky JTI (Joint Technology Initiative) is the umbrella project in which the GRC (Green RotorCraft) programme is embedded. The goal of Cleansky is the improvement of the environmental friendliness of aircraft. This means for GRC to reduce the overall CO_2 emmission, as well as the noise impact measured in $EPNL$ and complying with the current and future safety regulations. In GRC 1, innovative rotorblades are investigated using active and passive technologies to improve the blade performance itself and to meet the aforementioned goals. DLR contributed in both categories; on the one hand Riemenschneider et al. [1] test an active blade twist mechanism on a rotor blade, while on the other hand Imiela and Wilke [2] focus on the aerodynamic optimization of blade planform and twist of the rotorblade. This paper reflects the continued effort of the planform optimization by applying novel methodologies developed by Wilke [3] to obtain even better blades.

In the field of numerical rotor optimization in aerodynamics, many different approaches exist. The complexity of the rotor aero-mechanics calls for non-trivial simulations strategies. The flow field of the rotor is dominated by vortices spiced up with transonic and stalled regions, which, when everything is to be modelled correctly, calls for expensive high-fidelity CFD simulations. Additionally taking into account the unsteady nature and aero-elastic effects of the rotor, the computational effort is tremendous. On top of this, numerical optimization requires many evaluations and thus designing a rotor blade with the help of automized frameworks becomes a weary undertaking.

Therefore many research activities exist to cut down the computational costs. Dumont et al. [4] demonstrate that by applying the adjoint methodology to a gradient based optimization of a hovering rotor that the cost compared to evaluate the gradients directly with CFD is significantly reduced. Massaro and D'Andrea [5] take a different route and develop a simulation method based on potential theory with additional measures to take into account viscous effects to circumvent the need of CFD simulations in the optimization. This enables them to perform multi-point optimizations with a genetic optimization algorithm. Visingardi et al. [6] also perform an intensive optimization applying simplified aerodynamic models to have good turn-around times and compute objectives in ten different flight conditions. Other researches such as Johnson [7] and Imiela [8] employ surrogate based approaches to optimize rotor blades in hover and forward flight conditions. The surrogate based optimization aids the search for the optimum by generating a mathematical abstraction from the original simulation, which is then evaluated a lot faster than the original computed code.

Collins [9] was the first to join both strategies together; the use of surrogate models with high-fidelity CFD and low-fidelity models. This methodology is also referred to as multi- or variable-fidelity approach. First, a low-fidelity surrogate model is generated, where many simulations can be executed at low cost thus obtaining a highly accurate surrogate model (at low-fidelity level). Then, this model is re-calibrated with a few high-fidelity samples to arrive at the global high-fidelity optimum faster than only creating the high-fidelity surrogate purely from high-fidelity samples. Wilke [10] performs studies on which aerodynamic models are most suited for this type of optimization and further refined his variable-fidelity framework for multi-objective problems [3]. Latter work also underlined the need for the application of multi-objective strategies for the optimization of rotorblades, as single-objective optimized blades, either for hover or forward flight, tend to have drawbacks in the other flight condition. Leon et al. [11] introduces the Nash game approach to rotor blade optimization, which is further refined in [12], also speeding up their optimization with multi-fidelity methods. The Nash game may be (very) briefly summarized as a gradient based method, which starts at the best configuration of one objective and then gradually moves along the

Pareto front towards the other objective. Another multi-objective technique taking advantage of multiple fidelities is applied by Leusink et al. [13]. They start a genetic optimization at low-fidelity level, where they shrink the design space after an initial optimization. The obtained low-fidelity population from the second optimization is then resampled with the high-fidelity to create a high-fidelity surrogate model, in which the optimization is continued. They, however, do not update their high-fidelity surrogate model with novel designs, simply to avoid extensive use of computational resources.

The multi-objective approach proposed by [3], which was applied to a model rotor problem with few parameters at mid-fidelity level, is now applied to the reference rotor blade of the GRC 1 project. Here, the number of design parameters is increased from four to ten and additionally the pitch link loads are constrained in both flight conditions to arrive at more feasible blade planforms. The final results are already at high-fidelity level, thus no re-computation is necessary. A subset of the Pareto optimal configurations is abstracted and investigated in off-design conditions to further stress the need for multi-objective optimizations. Besides purely considering the aerodynamic performance, the rotors are also analyzed in a high-speed impulsive noise overflight condition required for certification.

2 METHODOLOGY

In Figure 1, a sketch of the overall optimization process is given. First, the baseline geometry is parameterized with ten design variables. The optimization is then started with a low-fidelity design of experiments. The design of experiments samples randomly different rotor geometries to then generate the first initial low-fidelity surrogate models ($\hat{y}_{lfm}$) of the returned goal functions and constraint values, here the required power in hover and forward flight along with their maximum pitch link loads. Within this surrogate model a multi-objective search is performed which generates a new choice of samples to be evaluated with the low-fidelity. Upon iterating the process a final low-fidelity surrogate model is obtained, from which the high-fidelity design of experiments is generated. To include a greater variety, random samples are additionally included to avoid a too strong bias with the low-fidelity optima in case these are not matching with the high-fidelity optima. With the first high-fidelity samples evaluated, the variable-fidelity surrogates are build ($\hat{y}_{vfm}$) which are then refined with a goal function refinement of each flight condition. These are basically two individual single-objective optimizations, which are simply coupled by also fulfilling the constraints of the opposing flight condition. This is done to find the anchor points of the Pareto front, before the actual high-fidelity multi-objective search is started to have a well-conditioned initial performance landscape. Upon completion of this process, the Pareto front of the high-fidelity sampled configurations is generated.

For the reference, the same process is repeated without using the low-fidelity at all, thus starting from a completely random design of experiments. The goal is to compare the performance of the single- to the variable fidelity approach. In the context of multi-objective optimization, the performance cannot be put into hard numbers, but is compared by the density and distribution of the final samples of each approach to judge the performance.

In the following, the individual parts of the optimization procedure are described; the design of experiments, the type of surrogate models, the optimization strategy within the surrogate model and the aerodynamic models applied.

2.1 Design of Experiments

The design of experiments plays an important role in setting up a surrogate based optimization. It can be related to a computational mesh in CFD. A bad mesh will not allow for good results, even if the solution scheme is of high-order. The same is true for the design of experiments; a bad initial surrogate model from an ill-conditioned design of experiments cannot be recovered by a highly accurate surrogate model. Romero et al. [14] study different types of design of experiments and based on this study, it is decided to use the central voronoi tesselation (CVT), see Ju et al. [15], for purely random design of experiments.

From the investigations in [3] it was seen that when creating high-fidelity design of experiments, it is beneficial to simply quick start the optimization with the optimum of the previous fidelity. However, this design space consists only of four parameters, which contains less local minima than the ten dimensional space. Therefore, a blend of low-fidelity optima, one from hover and from forward flight, is sampled along with a CVT cube. The single-high-fidelity is purely sampled with a CVT cube. The actual sample numbers for each fidelity and process can be found in Figure 2. Figure 2 also lists the numbers for the multi-objective update cycles as well as the the goal function refinement cycle, which are kept the same for single- and variable-fidelity.

2.2 Surrogate Models

The here employed surrogate models are based on Kriging. Kriging models a Gaussian process. On an abstract level, Kriging is a combination of a trend function and an error correction term:

$$\hat{y}(\vec{x}) = \hat{f}_{trend}(\vec{x}) + \epsilon(\vec{x}) \tag{1}$$

with $\hat{y}(\vec{x})$ the surrogate function, $\hat{f}_{trend}(\vec{x})$ is the trend function and $\epsilon(\vec{x})$ the error correction term. The most widely form of Kriging is universal Kriging, where the trend function is modelled by a polynomial. Exemplary for a one dimensional, second order surrogate this is written as:

$$\hat{f}_{trend}(x) = \beta_2 x^2 + \beta_1 x^1 + \beta_0 x^0 \tag{2}$$

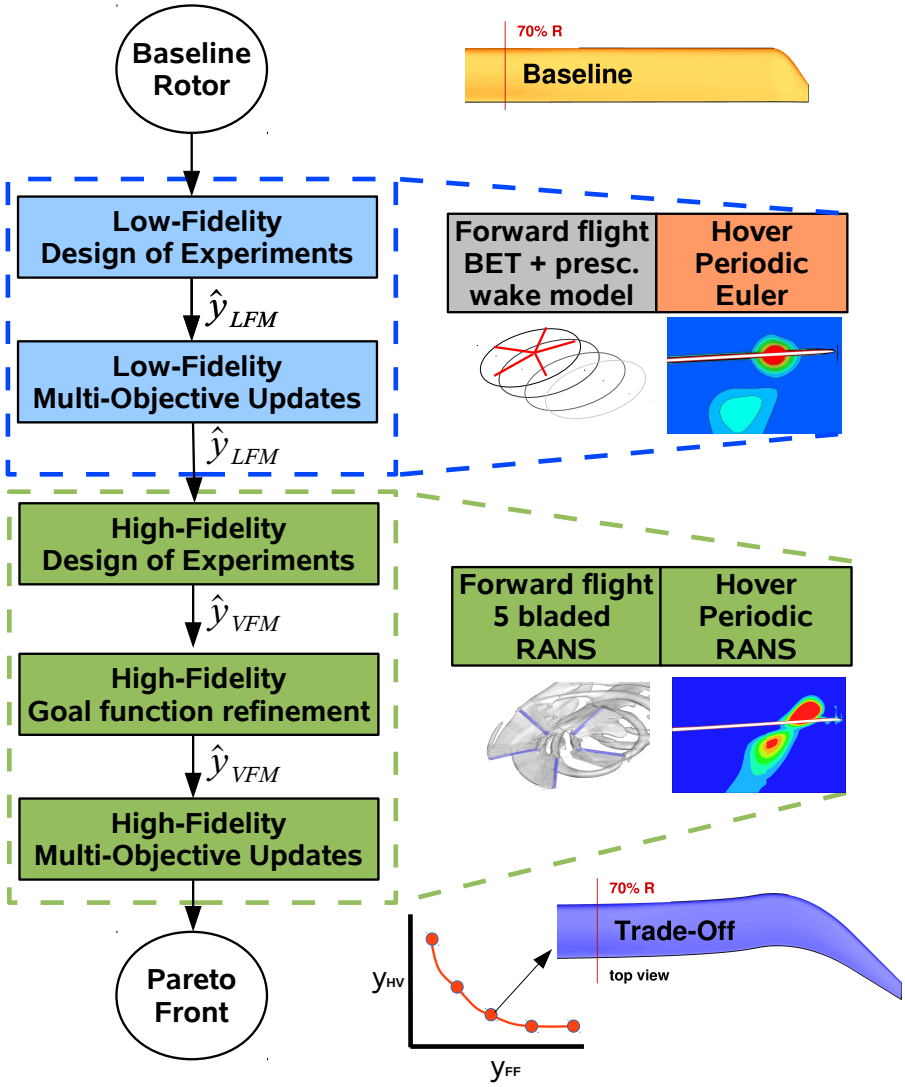

Figure 1: *Propsed multi-objective variable-fidelity optimization process for helicopter rotorblades. Left: the optimization process, right: blade geometries and simulation methodologies.*

with β_2, β_1 and β_0 the coefficients to be determined. In a more general, vectorial form it is written as:

$$\hat{f}_{trend}(x) = \vec{\beta} \cdot \vec{f} \tag{3}$$

where $\vec{\beta}$ contains the coefficients and $\vec{f}$ the regression vector. The error term is (usually) made of radial basis functions. These correct the offset between sampled points and the trend function:

$$\epsilon(\vec{x}) = \vec{\psi}(\vec{x})\mathbf{\Psi^{-1}}(\mathbf{X}_s)(\vec{Y}_s - \mathbf{F}(\mathbf{X}_s) \cdot \vec{\beta}) \tag{4}$$

with $\vec{\psi}$ the correlation vector between new sample points $\vec{x}$ and the given points $\mathbf{X}_s$, $\mathbf{\Psi}$ the correlation matrix of the sample points and $\mathbf{F}$ the regression matrix, which is made of all regression vectors generated by the samples $\mathbf{X}_s$. From the derivation of Kriging, the determination of the coefficients $\vec{\beta}$ is done by a generalized least squares method:

$$\vec{\beta} = (\mathbf{F}^T \mathbf{\Psi}^{-1} \mathbf{F})^{-1} \mathbf{F}^T \mathbf{\Psi}^{-1} \vec{Y}_s \tag{5}$$

For more detailed information on Kriging, the reader is referred to the book by Forester et al. [16]

While universal Kriging is a single-fidelity model, it is easily enhanced to a variable-fidelity model. The proposed Hierarchical Kriging by Han and Görtz [17] is based on the idea to exchange the trend function by a low-fidelity surrogate model, which may be based on universal Kriging or another Hierarchical Kriging for staged fidelity levels. The low-fidelity trend function is implemented in a slightly modified way in contrast to Han and Görtz and reads:

$$\hat{f}_{trend}(\vec{x}) = \rho \hat{y}_{lfm}(\vec{x}) + \sum_k^d (\beta_k x_k) \tag{6}$$

Where the low-fidelity model $\hat{y}_{lfm}$ is scaled by the parameter ρ and a multi-linear function $\sum_k^d (\beta_k x_k)$ is added on top to give more flexibility to the model. The coefficients ρ and β are determined just as in Eq. (5) for the polynomial trend. The parameter ρ is also a measure

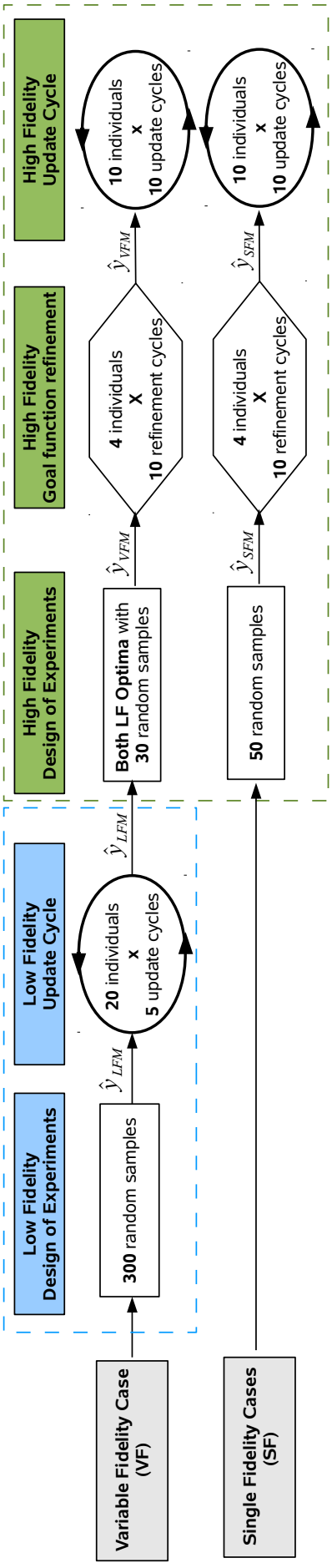

Figure 2: *Ressource allocation for variable- (VF) and single- (SF) fidelity optimizations.*

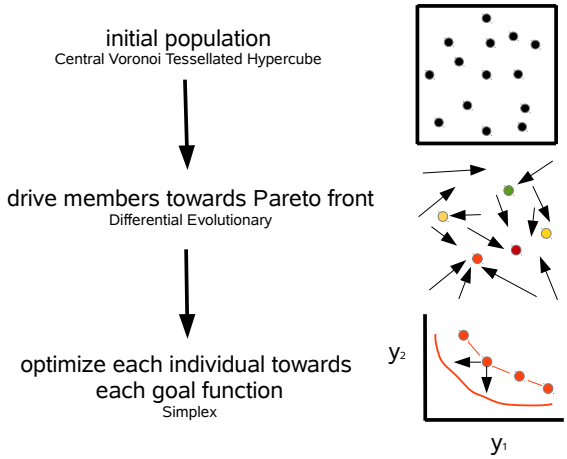

Figure 3: *Optimization strategy*

to see how well the high- and low-fidelity models match together. Values between $0.5 - 1.5$ show a good agreement, larger or smaller values may lead to the question if the low-fidelity method represents the same physics as the high-fidelity method.

2.3 Optimization Strategy

The optimization is done in three steps as shown in Figure 3. First a design of experiments is generated to create a good initial population for the following evolutionary algorithm. The Pareto front obtained by the evolutionary algorithm is then refined with a local, gradient-free search algorithm. This is done by starting multiple instances of the simplex algorithm at the locations of individuals and driving them towards both goal functions.

The here applied differential evolutionary (DE) algorithm originally developed by Storn and Price [18] is implemented in the global-local (DEGL) flavor by Das et al. [19] and extended with the non-dominated sorting genetic algorithm II (NSGA-II) [20] for multi-objective problems. The idea of the evolutionary algorithm is to model a naturaly evolving process which recovers the most fit individual at the end of the evolution. In contrast to genetic algorithms, the DE algorithm does the manipulation of individuals through vector operations. The global-local extension takes into account the globally best individual as well as an individual close to the mutated individual. This grants a faster convergences relative to the original DE algorithm. The fitness of each individual is then determined with the NSGA-II, where ranks and distances are assigned to individuals to specify their fitness.

The local searcher is the simplex algorithm by Nelder and Mead [21]. It is highly robust and is based upon the idea of moving a simplex through the optimization landscape, which shifts its vertices according to the goal function values. For the multi-objective optimization it is started at each individual from the DE algorithm and advances towards either goal function. All the points evaluated along the way are recorded and later on checked

for Pareto optimality to yield a more refined front than the differential evolutionary algorithm allowed.

This search mechanism is limited to finally yield a maximum of 1000 individuals in the end. As sampling all these with a high-fidelity is not considered economically, a reduction is performed first. The smallest distance to any existing sample is computed for each new individual and they are sorted in descending order. The top ten are then chosen for evaluation. This is repeated ten times to arrive at a refined surrogate model. This is different from the approach in [3], where the locations with the highest combined model error are chosen. This approach circumvents the problem of unintentionally weighing the error of one goal function more than the other and avoids abundant sampling in already well sampled areas.

The treatment of constraints in the multi-objective context is achieved by checking the constraint value in its respective surrogate model and whether the constraint is violated or not. If it is violated, the individual is considered unfit and receives very large goal function values, thus effectively eliminating it from the population or diverting the simplex algorithm. An implicit and maybe trivial constraint is enforced; the functionality of the rotor. If the aero-mechanic code returns that the configuration cannot fly due to the lack of lift or aero-elastic divergence, the constraint is considered violated, otherwise the rotor passes. This binary result of violated (1.1) or non-violated (0.0) is recorded in an additional surrogate model referred to as 'crashmap'. If this surrogate model returns a value larger than 1, the considered (surrogated) individual is considered unfit. The advantage of this error treatment is that no penalization or tainting of the goal function surrogate is necessary as no value needs to be inserted into it. The point is simply avoided by its existence in the crashmap.

2.4 Simulation Framework

The simulation process used for the high-fidelity simulations, but also partially for the low-fidelity is sketched in Figure 4. The pre-processing generates a discretization for the aero-mechanical code HOST [22] and the flow solver FLOWer [23]. For the HOST part, the properties of the aerodynamic quarter chord are inserted, such as chord length, sweep, anhedral and twist as well as the structural properties are adjusted. The approach by Stanger et al. [24] is integrated, where the stiffness properties are modified from the baseline blade according to scaling factors. The neutral and elastic axis, as well as the center of gravity are moved accordingly by the offset between reference and new blade. The disadvantage of this approach is that the dynamic and structural properties are not necessarily well conditioned for the given blade, but the advantage is that they can be computed based on the properties of the reference blade without specific knowledge of the interior of the reference blade. The pre-processing of FLOWer is the mesh generation accomplished by an in-house grid generator. The mesh generator is based on transfinite interpolation, similar to GEROS [25]. Then HOST is run, computing the aerodynamics based on tabled coefficients and determines the according blade movement and deformation to match the given trim condition. Upon convergence, the blade movement and deformation is communicated to FLOWer. FLOWer then computes the aerodynamics loads on the rotor blades, which are then updated in HOST during the next step. Not executed during the optimization, but later on in the acoustic evaluation of the selected rotor blades, DLR's Ffwocs-Williams Hawkins code APSIM [26] is run. It takes the porous surfaces written out during the last FLOWer run, which contain the flow variables from around the blade and evaluates the sound pressure level on a user defined carpet. For overflight noise computations, the sound carpet is a hemisphere, which is further processed by the tool HEMISPHERE [27] to determine the Effective Perceived Noise Levels (EPNL) on the ground. The size of the hemisphere is five time the rotor radius and is placed below the rotor.

2.4.1 Hover Simulations

Hover simulations are carried out either as inviscid Euler computations on a coarse mesh (low-fidelity) or as viscous RANS computations on a fine mesh (high-fidelity). The flight condition is modelled as a steady flow condition with periodic boundaries around the single-blade mesh to account for the influence of the other blades. To avoid growing the farfield to far out, the Froude boundary condition [28] is applied on the top, bottom and outer walls of the mesh. The Froude boundary condition sets the velocities at the farfield based upon the momentum theory of hovering rotors for the currently evaluated thrust and given disc area. A sketch of the meshes is displayed in Figure 5. An iso-surface of the vorticity is plotted in both pictures at the same magnitude. It is seen that the finer Navier-Stokes mesh conserves the tip vortex as well as the downwash longer than the coarser Euler mesh. In Table 1, the mesh sizes are listed in numbers. An additional note; only the Navier-Stokes mesh models the trailing edge tap, as the inviscid simulation has troubles in simulating the effects of the tap. The turbulence model is the $k-\omega$-SST model by Menter [29]. The factor in computational cost between the inviscid Euler computation and the viscous RANS simulation is roughly 35 meaning that 35 Euler computations can be executed for the same cost of one RANS simulation.

2.4.2 Forward Flight Simulations

The forward flight is modeled with the blade-element theory combined with a prescribed wake model [30] as the low-fidelity and a five bladed Chimera [31] setup in forward flight using RANS simulations. For the fast advance ratio to be modeled, three wake revolutions were kept within HOST to account for the influence of the wakes. As the fluid-structural coupling is based on a harmonic approach, a periodic solution needs to be obtained for the RANS simulations, before the loads can be exchanged with HOST. It has been determined that running the zeroth coupling step for a full revolution and then reducing this period by 72^o to 144^o of the full rev-

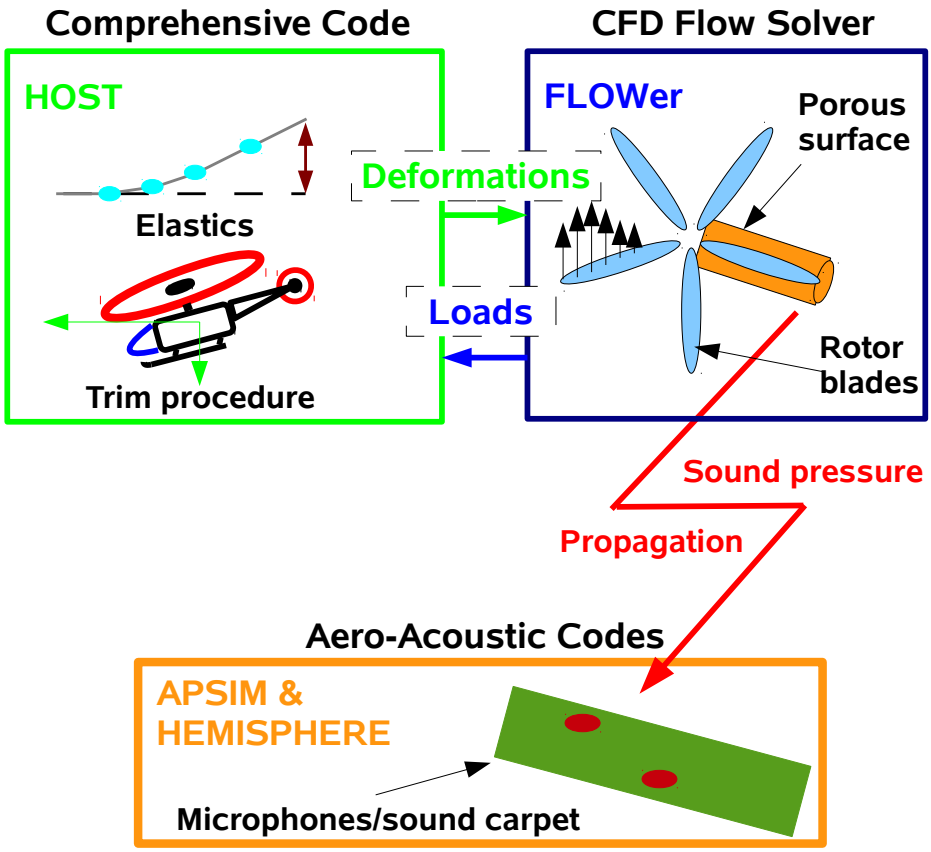

Figure 4: *Simulation Environment*

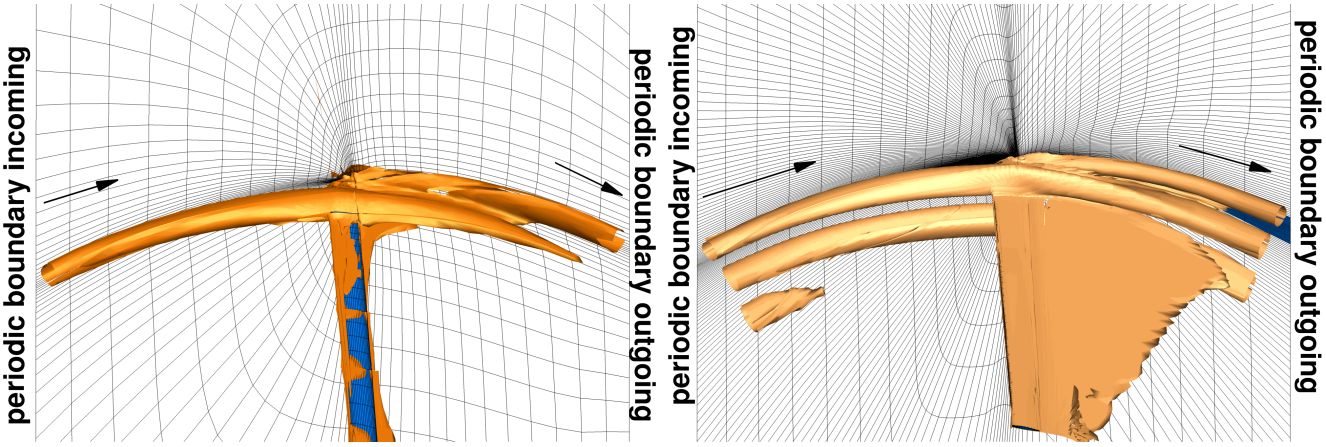

Figure 5: *Hover meshes. Left: coarse mesh for inviscid compuations, right: fine mesh for viscous compuations. NOTE: the increased vortex conservation on the finer mesh relative to the coarser mesh.*

case	hover			forward flight		
locations	radial	chord	azimuth	radial	chord	azimuth
Euler /	37	57		31		5
BET+ presc. wake	110,592 cells			30 panels		
RANS	73	185		65	113	0.5
	1,440,768 cells			13,025,280 cells		

Table 1: *Discretization of the blade for the individual solvers and flight conditions. Azimuth refers to the temporal resolution meassured in degrees of a revolution.*

olution granted a good compromise between accuracy and cost. The trim procedure ends either after 7 coupling steps or if the required power of the rotor changes less than 10^{-3} relatively. This results in an average of 5 coupling steps among the performed simulations. The discretization numbers of the forward flight simulations can also be taken from Table 1. The cost ratio of the high- to low-fidelity is 187,000 (!).

3 APPLICATION OF VFM BASED OPTIMIZATION

3.1 Reference Blade and Parameters

The described variable-fidelity optimization methodology is applied to the GRC reference rotor. The reference rotor depicted in Figure 7 is similar to the model rotor 7AD blade [32]. The blade features a linear twist distribution and a parabolic blade tip just as the 7AD, but does not employ any anhedral. The rotor itself has five blades with a tip radius of 5.5 m. The two flight conditions investigated are hover and forward flight. In hover, the thrust coefficient is $c_T/\sigma = 0.09$ and in forward flight $c_T/\sigma = 0.07$. The advance ratio in forward flight is $\mu = 0.33$, the tip Mach speeds are $M_{tip} = 0.65$ and $M_{tip} = 0.6$ in hover and forward flight respectively. The thrust is trimmed in hover, while in forward flight a set fuselage drag and required lift are trimmed along with the rolling moment.

The torque distribution in forward flight of the baseline blade is plotted in Figure 8, while the lift- and torque distribution in hover are plotted in Figure 9. In forward flight, this blade draws most of its power at the outer radial stations on the retreating blade side and in the rear part. Here, the airfoils operate at high angles-of-attack (AoA) to keep the helicopter in balance. A small sharp red line is identified on the advancing side, which is attributed to transonic effects. In hover, the lift grows linearly to about 80% r/R and then shows a curved peak at about 95%. This behavior comes from the tip vortex of the previous blade, which hits the blade at about 90% r/R. On the one side it increase the lift, on the other it decreases it. The wiggles in the torque distribution are also reasoned with the effect of tip vortices, yet the effect of the self-induced vortex is noted by the additional wiggle towards the tip. This comes from the parabolic blade tip, where the self-induced vortex starts when the leading-edge retreats. The acoustic footprint of the blade onto the hemisphere is drawn in Figure 10. Most sound is generated on the advancing side at the blade tip, which is coming from the mild shocks on the blade. Another region is identified on the retreating side, which is related to the higher loading of the blade tip in this area.

The rotor blade is parameterized with non-rational uniform B-splines (NURBS) [33]. Five twist parameters are chosen along with two sweeping and two tapering parameters and an an-/dihedral parameter. The great number of twist parameters is chosen as the blade twist is the most beneficial and simplest to accommodate parameter, while the an-/dihedral creates the greatest difficulties from a structural point of view. A picture of the placement of the parameters is given in Figure 6, where all NURBS control points are line markers, yet the ones free to modify by the optimizer are circled in magenta with arrows showing their degree of freedom.

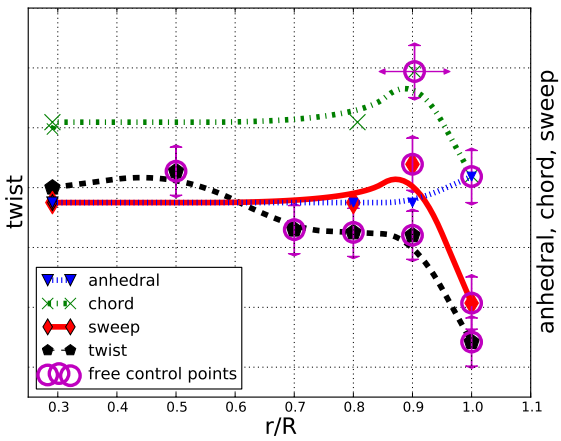

Figure 6: *Parameterization of GRC blade*

3.2 Optimization Results

The results after running the single- and variable-fidelity optimizations are displayed in Figure 11. On the left, the Pareto fronts obtained by either the single- ($\triangle$) or variable-fidelity ($*$) are depicted by the red and green line and markers, respectively. When combining both set of points together, the theoretical combined Pareto front ($\bullet$) is colored in magenta. The single-fidelity procedure found a total of 15 points and the variable-fidelity 17 points. However, the variable-fidelity is mostly more advanced than the single-fidelity. Therefore, if the contributions of both methods is compared to the combined front, only 4 points are from the single-fidelity and 13 from the variable-fidelity, thus the variable-fidelity retrieved 325 % more interesting points than the single-fidelity. Comparing the costs of both approaches, the single-fidelity evaluated slightly more high-fidelity points and thus has a total cost of 82.2 cpu years, while the variable-fidelity including the cost of evaluating the low-fidelity (0.15 cpu years) requires 74.4 cpu years. A cpu year is defined as the time it would take a single processor (XEON E5-2695 v2) to perform the presented optimizations. The overall gain of the variable-fidelity becomes evident.

3.3 Novel Blades for GRC

For the GRC 1 project, a subset of rotors obtained from these optimizations is chosen to be further studied. Three blades have been picked, namely the anchor points of each flight condition as well as an intermediate design. The blade performing best in forward flight, referred to as best forward flight blade is depicted in Figure 12, the best hover blade in Figure 20 and the intermediate choice, a trade-off blade, in Figure 16. Their respective

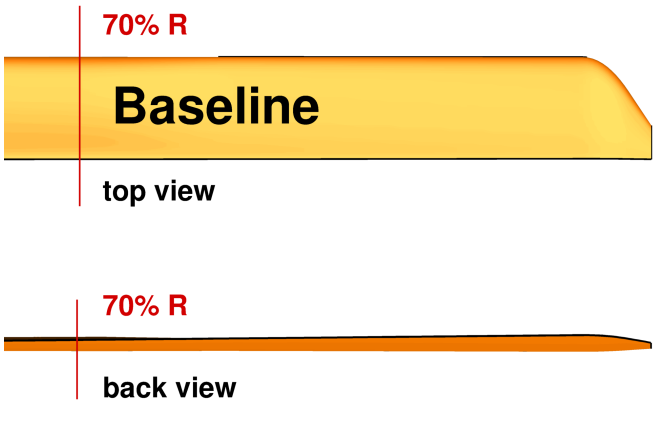

Figure 7: *Baseline blade*

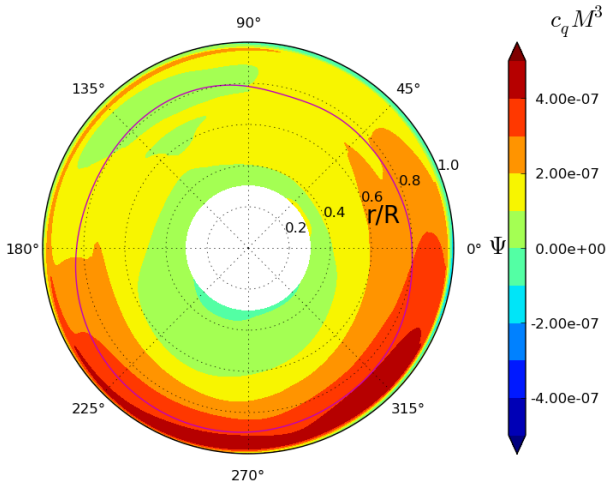

Figure 8: *Torque distribution of the baseline blade in forward flight.*

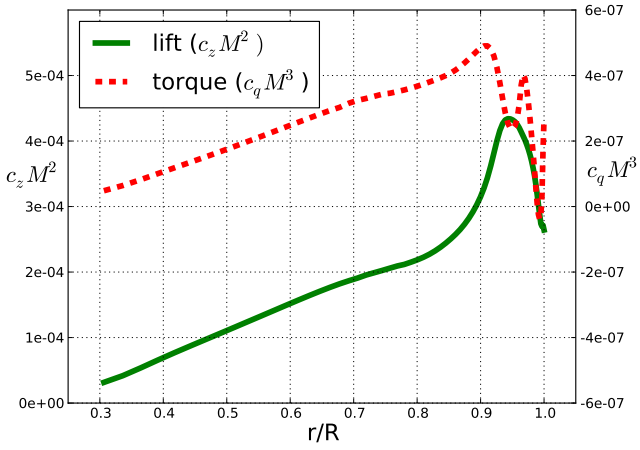

Figure 9: *Torque and lift difference distribution of the baseline blade in hover.*

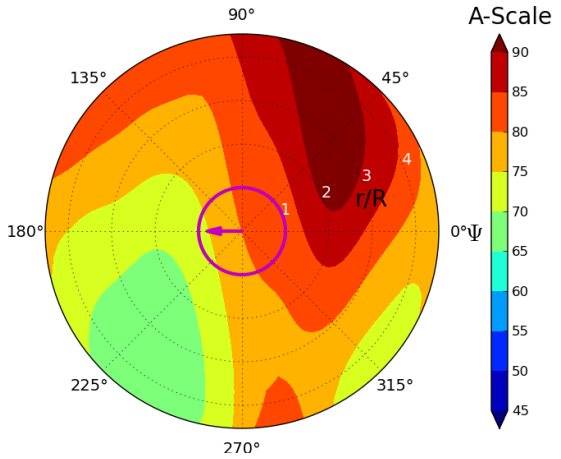

Figure 10: *Acoustic footprint on hemisphere of the reference blade.*

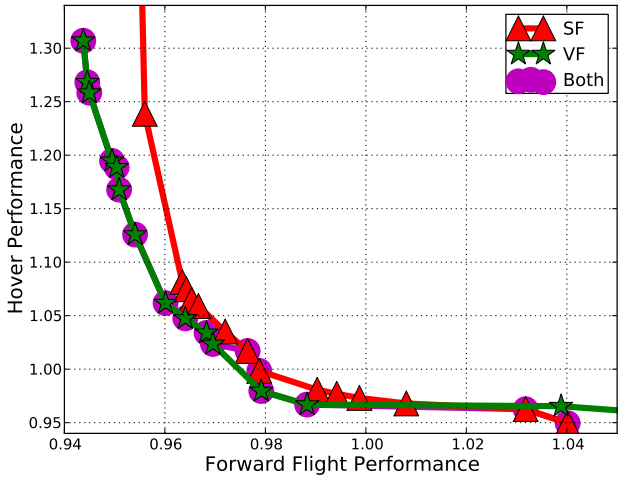

Figure 11: *Comparison of single-(SF) and variable-(VF) fidelity Pareto fronts and parameters obtained from high-fidelity multi-objective optimizations.*

performances in reference to the baseline blade are listed in Table 2. Their off-design performance is plotted in Figure 25 for hover and in Figure 26 as well in Figure 27 for forward flight.

3.3.1 Best forward flight blade

The best forward flight blade has little non-linear blade twist with an early tapered blade tip and sweeps the blade backward. A mild dihedral is found.

In forward flight, Figure 13, the small blade tip along with the decrease in the twist gradient beyond 90% r/R reduces the power requirements in the outer sections. At the inboard section of the blade a positive twist gradient is observed, which arises from alleviating the root vortex, which is seen at roughly 90^o azimuth at the inboard location. This is questionable as neither the hub nor the blade attachments are modeled and the strength and location of the root vortex are likely to be different on the complete configuration.

Moving onto the performance in hover, this is strongly degraded in contrast to the reference blade. In Figure 14 it is seen that the lift is strongly decreased beyond 90% r/R. The reason for this is that the flow separates in

Blade	forward flight		hover		overflight
	req. power	constraint	req. power	constraint	HSI-noise
Best Forward Flight	-5.9%	-12.4%	+30.7%	-23.8%	-3.3 dB
Trade-Off	-2.4%	-30.5%	-2.0%	-4.2%	-1.1 dB
Best Hover	+7.9%	-12.9%	-6.5%	-0.5%	+9.5 dB

Table 2: *Improvements of selected multi-objective rotors. HSI = High-Speed Impuslive*

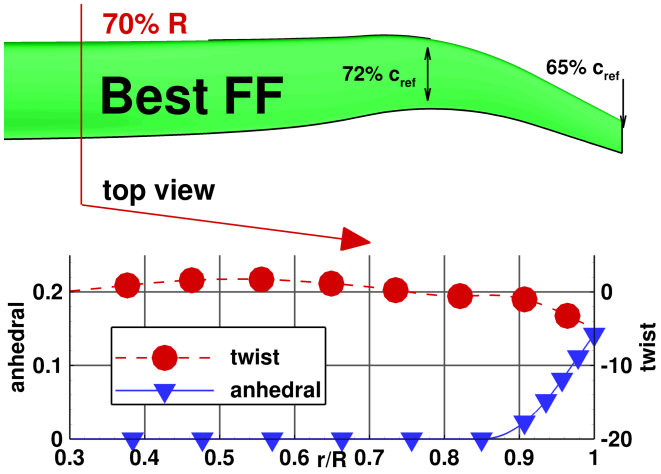

Figure 12: *Best forward flight blade*

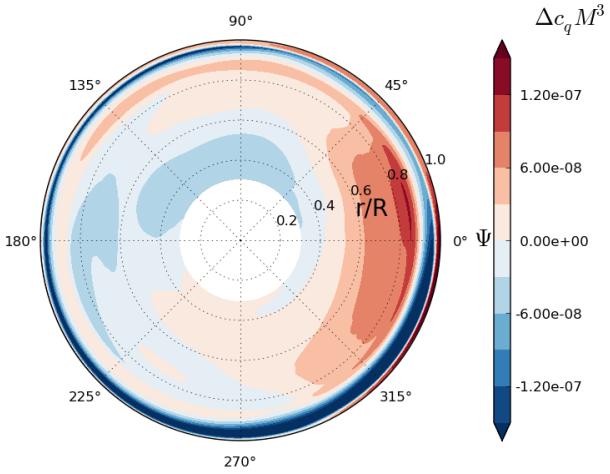

Figure 13: *Torque difference distribution of the best forward flight blade in forward flight.*

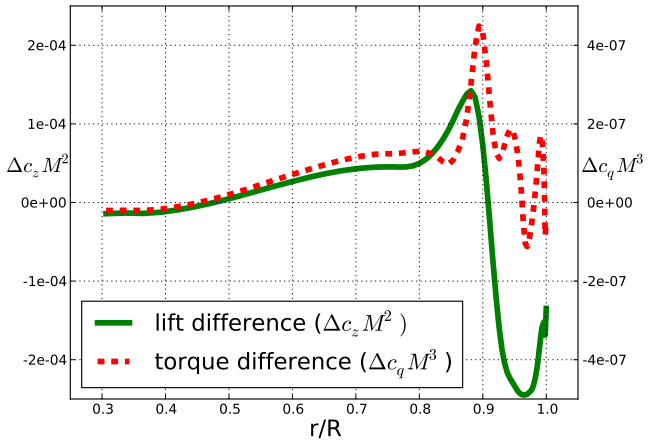

Figure 14: *Torque and lift difference distribution of the best forward flight blade in hover. Values above zero mean an increase in contrast to the reference blade.*

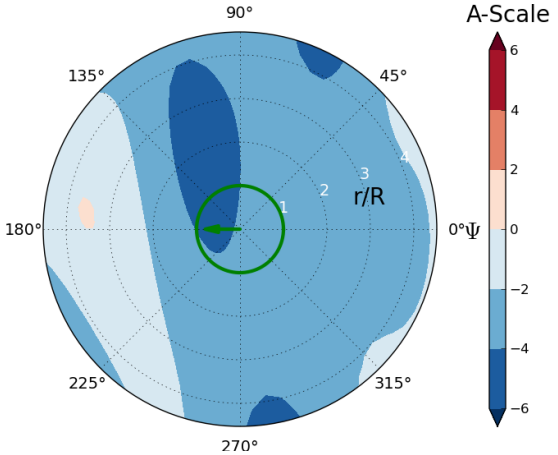

Figure 15: *Change of the acoustic footprint on hemisphere in contrast to the reference blade.*

Red means that the optimized performs worse than the reference blade, blue an improvement

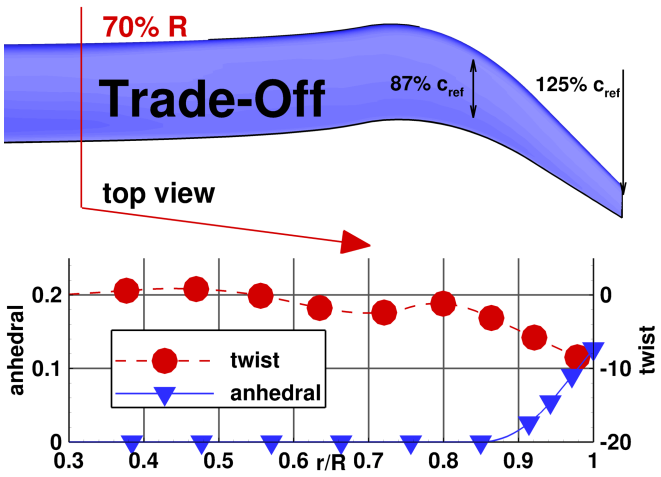

Figure 16: *Trade-off blade*

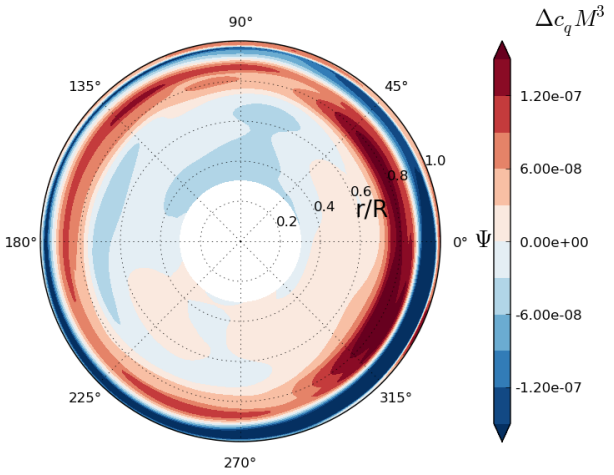

Figure 17: *Torque difference distribution of the trade-off blade in forward flight.*

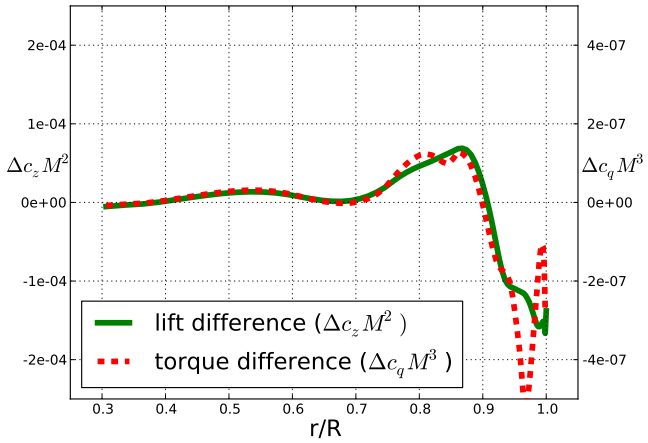

Figure 18: *Torque and lift difference distribution of the trade-off blade in hover. Values above zero mean an increase in contrast to the reference blade.*

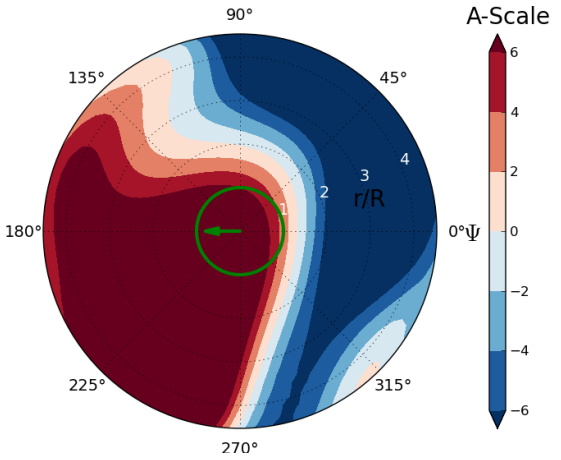

Figure 19: *Change of the acoustic footprint of the trade-off blade on hemisphere in contrast to the reference blade. Red means that the optimized performs worse than the reference blade, blue an improvement*

this region of the blade and thus more power overall is absorbed. The separation is attributed to the relatively low twist angle (high AoA) and small blade tip of this blade.

These findings are also reflected by the polar plots in Figure 25. The forward flight blade performs worse than the reference blade in the whole thrust domain, but in forward flight proves to be slightly superior as of Figure 26 and Figure 27. However, the gap between reference blade and best forward flight blade becomes smaller at higher velocities, which is an indicator that the small blade tip may not be beneficial at even greater advance ratios, as the required thrust may not be delivered.

The change of the acoustic footprint of the blade for the high-speed impulsive noise overflight procedure onto the hemisphere is plotted in Figure 15. The blade becomes quieter at the louder locations of the baseline blade. As the loud locations of the baseline blade are also the dominant drivers in the overflight noise, this leads to an overall decrease of 3.6 dB EPNL.

3.3.2 Trade-off blade

The trade-off blade is chosen from the set of Pareto optimal points as it features roughly the same improvement in both flight conditions. The twist towards the tip is further decreased, a larger dihedral is found, the blade is swept stronger and blade area is larger than the best forward flight blade. These effects lead to a degradation of forward flight performance in contrast with the best forward flight blade, but increases the hover performance.

The forward flight torque difference distribution plotted in Figure 17 reveals that the increase of the chord length as well as the slight bump of the twist distribution leads to an increased power consumption at 80% r/R throughout the revolution. This is also the area where more lift is generated in relation to the baseline blade and thus this section is traded off with the outer radial stations, where less power is consumed, which comes from the further decreased twist beyond the 90% r/R position.

The raised dihedral compared to the best forward flight blade as well as the greater twist offset at the tip

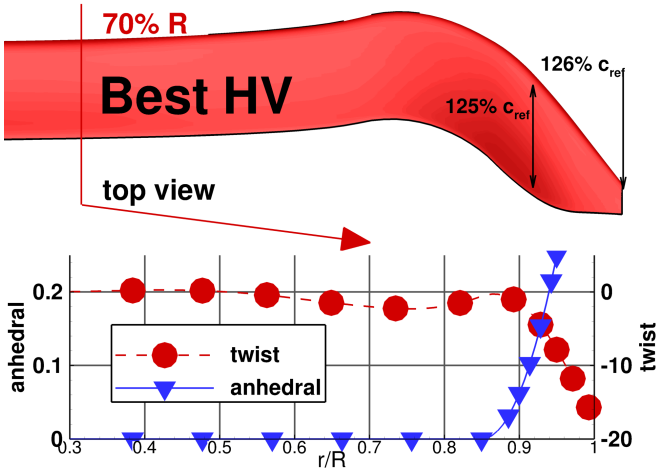

Figure 20: *Best hover blade*

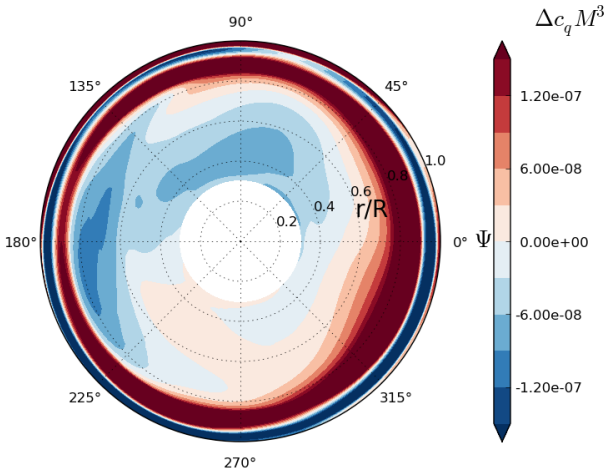

Figure 21: *Torque difference distribution of the best hover blade in forward flight.*

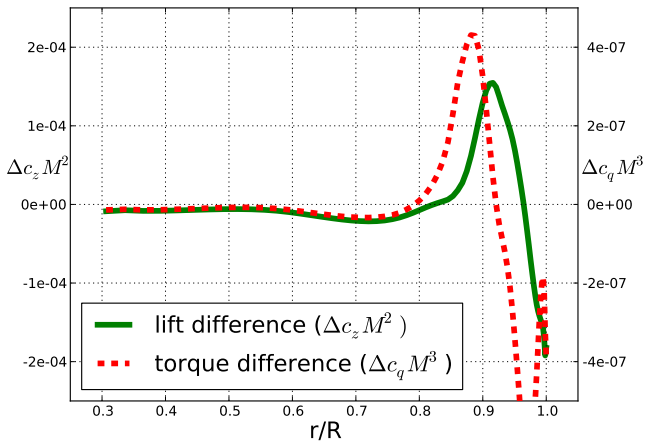

Figure 22: *Torque and lift difference distribution of the best hover blade in hover. Values above zero mean an increase in contrast to the reference blade.*
Red means that the optimized performs worse than the reference blade, blue an improvement

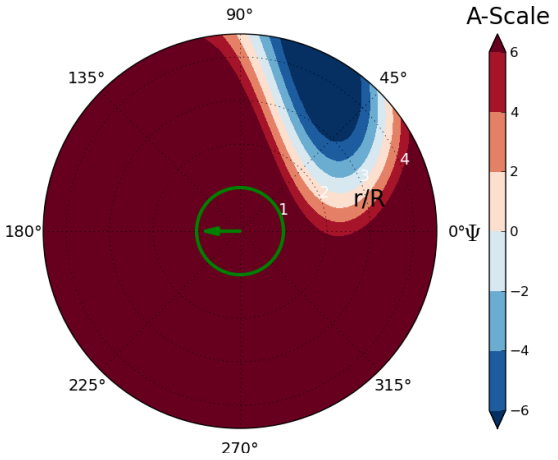

Figure 23: *Change of the acoustic footprint of the best hover blade on hemisphere in contrast to the reference blade.*

lead to a strong offloading of the blade at the tip in hover as seen in Figure 18. However, at 85% r/R, more lift as well as torque are generated, which is traced back to the bump in the twist distribution as well as the increase in the chord length at this location.

The off-design evaluation in hover, Figure 25, the blade surpasses the reference blade throughout the whole operational envelope, yet its peak performance is at a slightly lower thrust than the reference blade, despite the fact that the Figure of Merit is higher. At lower advance ratios in forward flight the trade-off blade is similar to the baseline blade, but becomes better towards the design point. The tendency goes back with higher velocities, just as observed with the best forward flight blade.

The acoustics of the blade in fast forward flight reduce the noise footprint on the ground by -1.1 dB when compared to the reference blade. Looking at Figure 19, the blade is quieter on the rear and advancing side of the revolution, but also a louder on the front and retreating side. The additional blade sweep in contrast to the reference blade reliefs the transonic regions, but leads to a greater generation of loading noise on the retreating side, which then in sum gives less improvement than the best forward flight blade has.

3.3.3 Best hover blade

The best hover blade features a very non-conservative twist distribution. While mostly close to zero up to 90% r/R, it sharply drops off towards the blade tip, only a slight bump at 85% r/R is noticed. The blade area is increased in contrast with the reference blade and the forward-backward sweeping is also more pronounced than it has been with the previous blades. A strong dihedral is attached to the blade.

From Figure 21 it is concluded that this blade is not made for forward flight conditions. A large torque increase around the 80% r/R position is found over the complete revolution being associated with the large tip area. The strong twist offset at the tip also shows benefits in this flight condition, but is too little to compensate for the losses caused by the enlarged chord distribution at the tip.

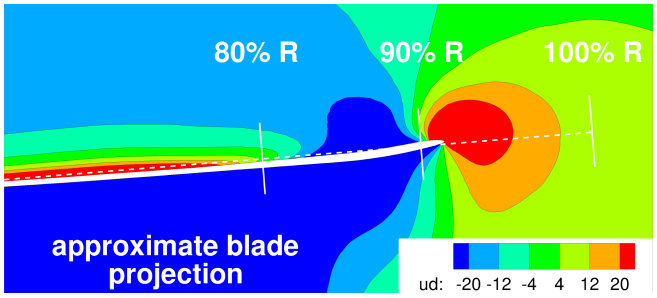

Figure 24: *Cut through the blade with plot of the axial velocity through the blade. Tip is at 100% R.*

From Figure 22 an interesting fact is discovered; the blade recovers energy from the flow beyond the 90% r/R. The reason for this is that the strong twist offset along with the blade sweep and dihedral cause this portion of the blade to be aligned in the upwind region of the previous tip vortex. The resulting force on the airfoils in that region is pointed forwards instead of backwards, similar to autorotation or windmill cases. In the downwind section of the previous tip vortex, the blade area is increased and the bump in the twist distribution is found, which compensates for the otherwise lost lift. This costs more drag, but with the recovery mechanism from the outer blade tip, the sum is less than with the reference blade. To illustrate the mechanism, Figure 24 pictures the locations of up and downwash caused by the blades as well as the previous tip vortex. Beyond 90% r/R a strong upwash is noticed, which allows for the energy recovery. Note, a perpetu mobile cannot be created with this mechanism, as the price for the tip vortex has to be paid first, before it can be exploited, which will always be higher than the actual recovery.

The off-design performance shows a reciprocal behavior to the best forward flight blade. In hover, Figure 25, the blade surpasses the reference blade over the whole thrust range and has its peak Figure of Merit well past the baseline blade, which would also make it suitable for heavy lifting. However, it is not suited for forward flight, as it draws more power over the complete velocity range, Figure 26. Unlike the other two blades, it decreases its gap with the reference blade at higher velocities, likely because a higher thrust is needed and the enlarged area might prove beneficial at greater advance ratios, if other issues such as aero-elastic divergence do not occur, Figure 27.

Evaluating the acoustic footprint on the ground in the high-speed overflight condition, the blade becomes a lot noisier than the baseline blade by 9.5 dB EPNL. This is related to the large tip area, which causes stronger transonic effects and when looking at the hemispherical sound distribution, it is seen that this makes the blade noisier in almost all regions, Figure 23

4 CONCLUSIONS

The multi-objective technique developed by Wilke [3] for the variable-fidelity optimization of helicopter rotor

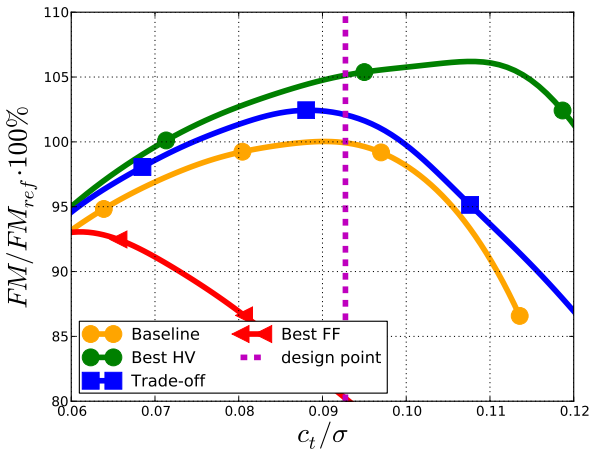

Figure 25: *Figure of Merit over thrust blade in hover*

blades has been applied within the Green RotorCraft research programme of CleanSky to design potential future blade designs.

This multi-objective approach revealed very promising results. First, it demonstrated that the application of variable-fidelity approaches leads to a much denser and advanced Pareto front than applying only one fidelity when using roughly the same amount of resources. Secondly, it underlined the importance to go with a multi-objective optimization strategy, as otherwise only blades are found that either optimize the hover or the forward flight condition, which lead to contrary designs. Thirdly, a set of three potential blade designs is retrieved and studied in further detail.

It is seen that the pure forward flight or hover blades actually perform worse in the opposing flight condition. The multi-objective approach allowed for a good trade-off to accommodate both. However, if helicopters were designed for single-purposes, or at least their rotor blades, the forward flight blade might be a promising design for fast VIP transport to remote regions. The hover blade might also be suited for heavy lifting for a helicopter of this class or long-endurance surveillance missions. The trade-off blade however, could be a potential successor to current blade designs, which are themselves already trade-offs between these two mission types. This blade also shows similarities to the ERATO design [34] despite the fact that latter has been optimized for acoustics.

Upon evaluating the sound emission of these blades in high-speed impulsive flight conditions, it was found that blade sweep is not the only answer to reduce the shock on the advancing side regions. The hover blade features the greatest blade sweep, however due to its thicker blade at the tip, it becomes overall louder than the other blades. The slim, yet only mildly swept blade for forward flight then proved to be the quietest blade among the ones investigated.

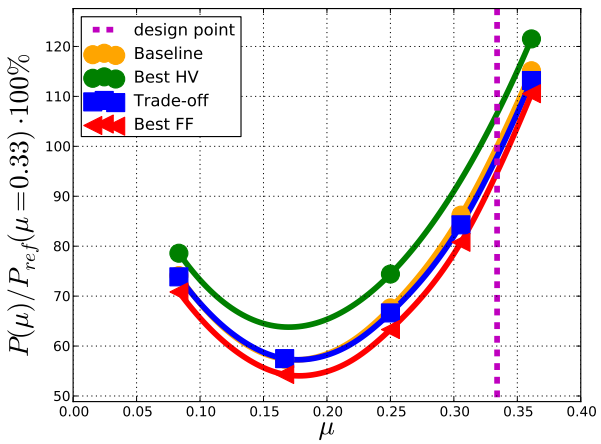

Figure 26: *Required power in forward flight for various advance ratios*

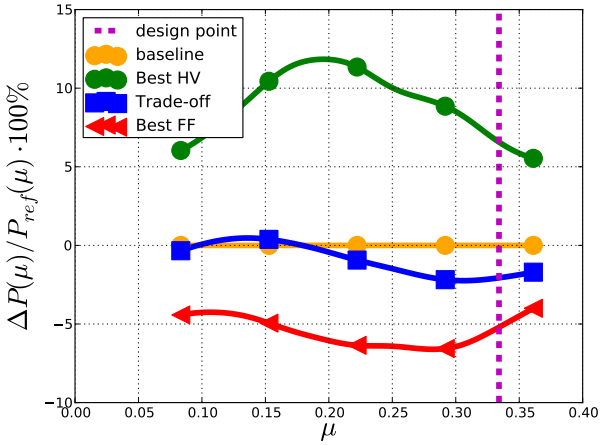

Figure 27: *Relative performance difference to reference blade in forward flight for various advance ratios*

5 AKNOWLEDGEMENTS

The research leading to these results has received funding from the European Community's Seventh Framework Programme (FP7/2007-2013) for the Clean Sky Joint Technology Initiative under grant agreement n^o CSJU-GAM-GRC-2008-001.

References

[1] J. Riemenschneider, R. Keimer, and S. Kalow: Experimental Bench Testing of an Active-Twist Rotor. In: *39th European Rotorcraft Forum*, 2013

[2] M. Imiela and G. Wilke: Passive Blade Optimization and Evaluation in Off-Design Conditions. In: *39th European Rotorcraft Forum*, 2013

[3] G. Wilke: Multi-Objective Optimizations in Rotor Aerodynamics using Variable Fidelity Simulations. In: *39th European Rotorcraft Forum*, 2013

[4] A. Dumont, A. Le Pape, J. Peter and S. Huberson: Aerodynamic Shape Optimization of Hovering Rotors Using a Discrete Adjoint of the Reynolds-Averaged Navier-Stokes Equations. In: *Journal of American Helicopter Society* 56 (2011), 032002-1-11

[5] A. Massaro and A. D'Andrea: Multi-Point Aerodynamic Optimization by Means of Memetic Algorithm for Design of Advanced Tiltrotor Blades. In: *39th European Rotorcraft Forum*, 2013

[6] A. Visingardi, L. Federico, and M. Barbarino: Blade Planform Optimization for a Dual Speed Rotor Concept. In: *38th European Rotorcraft Forum*, 2012

[7] C. Johnson: *Optimisation of Aspects of Rotor Blades using Computational Fluid Dynamics*, University of Liverpool, Dissertation, 2012

[8] M. Imiela: *Mehrpunktoptimierung eines Hubschrauberrotors im Schwebe- und Vorwärtsflug unter Berücksichtigung der Fluid-Struktur-Wechselwirkung*, Institut für Aerodynamik und Strömungstechnik Braunschweig, Dissertation, 2012

[9] K. B. Collins: *A Multi-Fidelity Framework for Physics Based Rotor Blade Simulation and Optimization*, Georgia Institute of Technology, Dissertation, 2008

[10] G. Wilke: Variable Fidelity Optimization of Required Power of Rotor Blades: Investigation of Aerodynamic Models and their Application. In: *38th European Rotorcraft Forum*, 2012

[11] E. R. Leon, A. Le Pape, J-A. Desiderie, D. Alfano, M. Costes: Concurrent Aerodynamic Optimization of Rotor Blades Using a Nash Game Method. In: *AHS 69th Annual Forum*, 2013

[12] E. R. Leon, J-A. Desiderie, A. Le Pape, and D. Alfano: Multi-Fidelity Concurrent Aerodynamic Optimization of Rotor Blades in Hover and Forward Flight. In: *40th European Rotorcraft Forum*, 2014

[13] D. Leusink, D. Alfano, and P. Cinnella: Multi-fidelity optimization strategy for the industrial aerodynamic design of helicopter rotor blades. In: *Aerospace Science and Technology* 42 (2015), Nr. 0, 136 - 147. – ISSN 1270–9638

[14] V. J. Romero, J. V. Burkardt, M. D. Gunzburger, and J. S. Peterson: Comparison of pure and "Latinized" centroidal Voronoi tessellation against various other statistical sampling methods. In: *Reliability Engineering & System Safety* 91 (2006), S. 1266–1280

[15] L. Ju, Q. Du, and M. Gunzburger: Probabilistic methods for centroidal Voronoi tessellations and their parallel implementations. In: *Parallel Computing* 28 (2002), S. 1477–1500

[16] A. Forrester, A. Sòbester, and A. Keane: *Engineering Design via Surrogate Modelling - A Practical Guide*. John Wiley & Sons Ltd., 2008. http://dx.doi.org/10.1002/9780470770801

[17] Z.-H. Han, and S. Görtz: A Hierarchical Kriging Model for Variable-Fidelity Surrogate Modeling. In: *AIAA Journal* 50-9 (2012), 1885-1896

[18] R. Storn, and K. Price: Differential Evolution - A simple and efficient adaptive scheme for global optimization over continuous spaces. In: *Journal of Global Optimization* 11 (1997), S. 341–359

[19] S. Das, A. Abraham, U. K. Chakraborty, and A. Konar: Differential Evolution Using a Neighborhood-Based Mutation Operator. In: *IEEE Transactions on Evolutionary Computation* 13-3 (2009), S. 526–

[20] K. Deb, A. Pratap, S. Agarwal, and T. Meyarivan: A fast and elitist multiobjective genetic algorithm: NSGA-II. In: *IEEE Transactions on Evolutionary Computation* 6 (2002), apr, Nr. 2, S. 182 –197. – ISSN 1089–778X

[21] J.A. Nelder, and R. Mead: A simplex function for minimization. In: *Computer Journal* 8-1 (1965), S. 308–313

[22] B. Benoit, A.-M. Dequin, K. Kampa, W. von Grünhagen, P.-M. Basset, and B. Gimonet: HOST, a General Helicopter Simulation Tool for Germany and France. In: *American Helicopter Society 56th Annual Forum, Virginia Beach, Virginia, May 2-4, 2000*, 2000

[23] J. Raddatz, and J. Fassbender: Block structured Navier-Stokes solver FLOWer. MEGAFLOW - Numerical Flow Simulation for Aircraft Design. In: *Notes on Numerical Fluid Mechanics and Multidisciplinary Design* 89 (2005), S. 27–44

[24] C. Stanger, M. Hollands, M. Kessler, and E. Krämer: Adaptation of the Dynamic Rotor Blade Modelling in CAMRAD for Fluid-Structure Coupling within a Blade Design Process. In: *18. DGLR-Fach-Symposium der STAB*, 2012

[25] C. B. Allen: CHIMERA volume grid generation within the EROS code. In: *Proceedings of the Institution of Mechanical Engineers, Part G: Journal of Aerospace Engineering* 214 (2000), 125-140

[26] J. Yin, and J. Delfs: Improvement of DLR Rotor Aeroacoustic Code (APSIM) and its Validation with Analytic Solution. In: *29th European Rotorcraft Forum,*, 2003

[27] J. Yin, and H. Buchholz: Toward Noise Abatement Flight Procedure Design: DLR Rotorcraft Noise Ground Footprints Model. In: *Journal of American Helicopter Society* 52 (2007), April, Nr. 2, S. 90–98

[28] P. Beaumier, C. Castellin, and G. Arnaud: Performance prediction and flowfield analysis of rotors in hover, using a coupled Euler/Boundary layer method. In: *24th European Rotorcraft Forum*, 1998

[29] F.R. Menter: Two-Equation Eddy-Viscosity Turbulence Models for Engineering Applications. In: *AIAA-Journal* 32 (1994), S. 1598–1605

[30] G. Arnaud, and P.Beaumier: Validation of R85/Metar on the Puma RAE Flight Tests. In: *18th European Rotorcraft Forum*, 1992

[31] T. Schwarz: *Ein blockstrukturiertes Verfahren zur Simulation der Umströmung komplexer Konfigurationen*, Institut für Aerodynamik und Strömungstechnik Braunschweig, Dissertation, 2005

[32] M. Allongue and J.P. Drevet: New rotor test rig in the large Modane wind tunnel. In: *15th European Rotorcraft Forum*, 1989

[33] Piegl, Les and Tiller, Wayne: *The NURBS Book (2nd Ed.)*. New York, NY, USA : Springer-Verlag New York, Inc., 1997. – ISBN 3–540–61545–8

[34] J. Prieur, J. and W. R. Splettstoesser: ERATO - An ONERA-DLR Cooperative Programme On Aeroacoustic Rotor Optimization. In: *25th European Rotorcraft Forum*, 1999